Supplementary Information

Van der Waals interfaces in multilayer junctions for ultraviolet photodetection

Shihong Xie[1,2,*], Mustaqeem Shiffa[1], Mujahid Shiffa[1], Zakhar R. Kudrynskyi[1], Oleg Makarovskiy[1], Zakhar D. Kovalyuk[3], Wenkai Zhu[2], Kaiyou Wang[2] and Amalia Patanè[1,*]

[1]School of Physics and Astronomy, University of Nottingham, Nottingham NG7 2RD, United Kingdom

[2]State Key Laboratory of Superlattices and Microstructures, Institute of Semiconductors, Chinese Academy of Sciences, Beijing 100083, China

[3]Frantsevich Institute for Problems of Materials Science, The National Academy of Sciences of Ukraine, Chernivtsi Branch, Chernivtsi 58001, Ukraine

*Correspondence should be addressed to

Shihong Xie (email: shihong.xie@nottingham.ac.uk) or

Amalia Patanè (email: amalia.patane@nottingham.ac.uk)

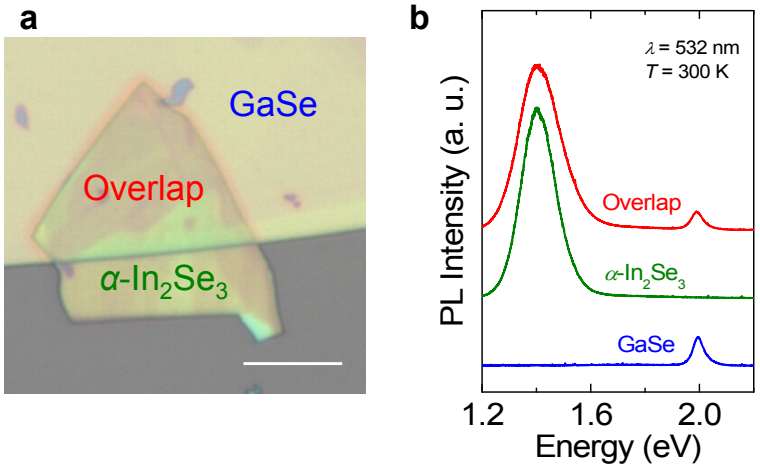

Supplementary Figure 1. Photoluminescence of ε-GaSe, α-In_2Se_3, and ε-GaSe/α-In_2Se_3 heterostructures. (a) Optical image of a GaSe/In_2Se_3 heterostructure. Scale bar: 10 μm. (b) Photoluminescence spectra (PL) of bulk In_2Se_3 and GaSe flakes, and their GaSe/In_2Se_3 overlapping area (T = 300 K, λ = 532 nm). The spectra show the band edge emission of In_2Se_3 and GaSe. The two emissions are centred at about 1.4 eV and 2 eV, respectively, as expected for isolated bulk layers.

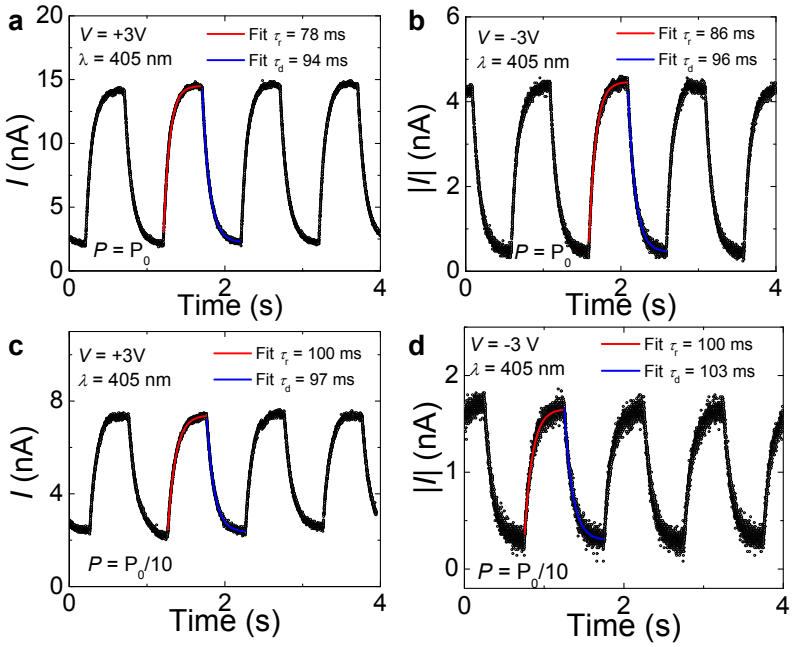

Supplementary Figure 2. Time-dependent photocurrent of a device. Temporal dependence of the current under illumination at λ = 405 nm, power (a-b) P_0 = 0.08 μW and (c-d) P_0/10 at different voltages V = ±3 V. The rise and decay times shown in these plots were estimated by fitting the data by $I(t) = I_0(1 - e^{-t/\tau_r})$ and $I(t) = I_0 e^{-t/\tau_d}$. The corresponding fits are plotted alongside the original dataset as red and blue lines.

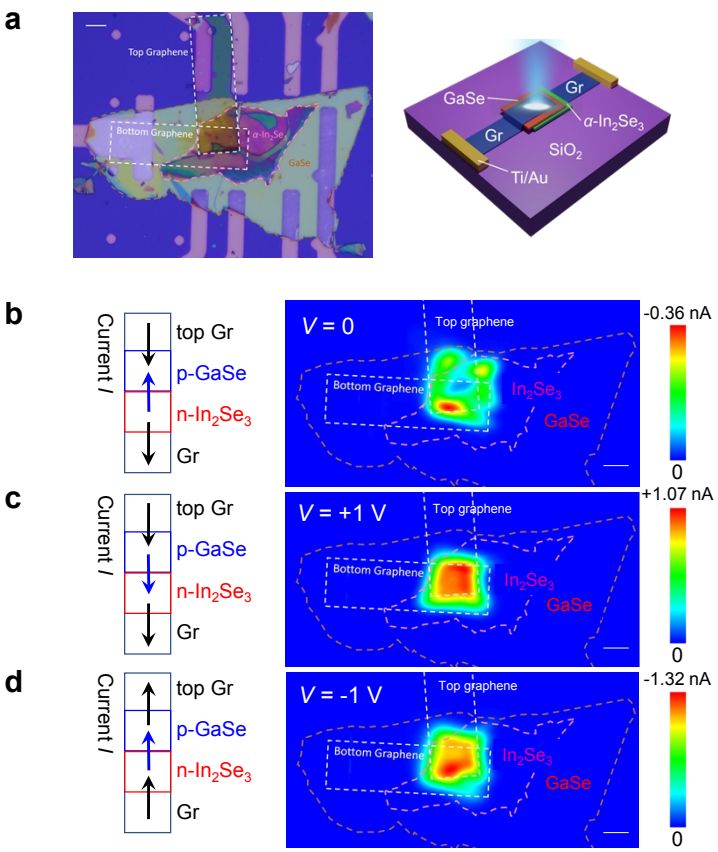

Supplementary Figure 3. A graphene-contacted *p*-GaSe/*n*-In_2Se_3 (30/30 nm) heterojunction. (a) Left: Optical image of the device. Right: Schematic of a graphene contacted *p*-GaSe/*n*-In_2Se_3 junction (30/30 nm). Scale bar: 10 μm. (b-d) Photocurrent (ΔI) maps at (b) $V = 0$, (c) +1 V and (d) -1 V. The laser beam ($\lambda = 425$ nm and $P = 15$ μW) has a spot size of about 1 μm. Scale bar: 10 μm. The left insets illustrate the direction of the current across the three interfaces of the heterostructure.

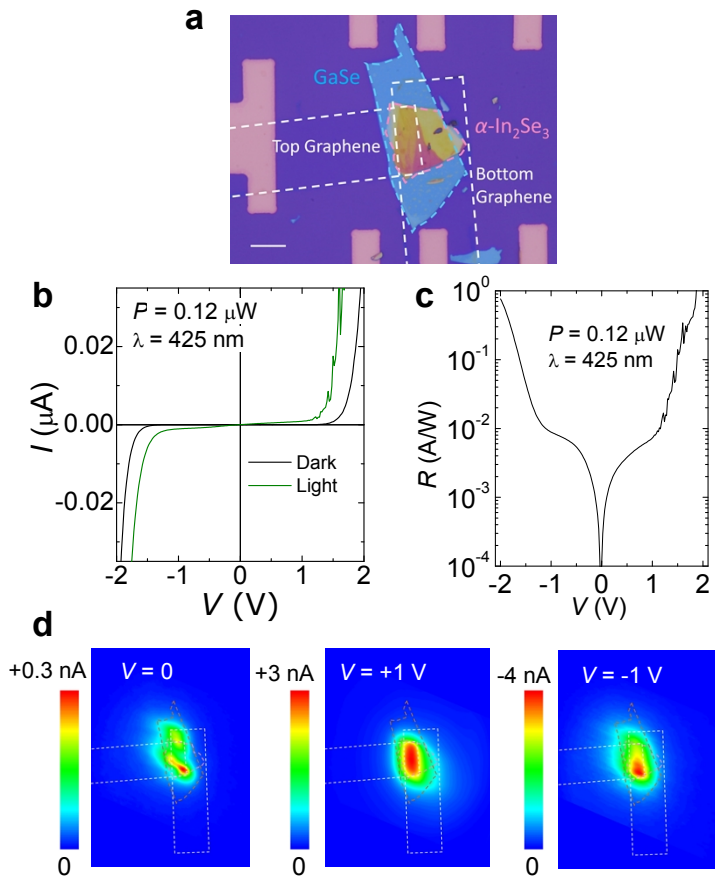

Supplementary Figure 4. A graphene-contacted *p*-GaSe/*n*-In_2Se_3 (10/20 nm) heterojunction. (a) Optical image of the device. Scale bar: 10 μm. (b) Current-voltage *I*-*V* characteristics in the dark and under illumination with $\lambda = 425$ nm ($T = 300$ K, $P = 0.12$ μW). (c) Photoresponsivity (R) versus V at $\lambda = 425$ nm ($P = 0.12$ μW) and $T = 300$ K. (d) Room temperature ($T = 300$ K) photocurrent (ΔI) maps at $V = 0$, +1 V and -1 V. The laser beam ($\lambda = 425$ nm and $P = 20$ μW) is focused by a microscope objective and the diameter of the spot size is around 1 μm. It can be seen that the photocurrent originates primarily from the region of overlap of the *p*-GaSe and *n*-In_2Se_3 layers with the bottom and top-graphene layers, rather than just the *p*-GaSe and graphene layers.

Supplementary Table 1. Comparison of device performance parameters for UV photodetectors based on Si or vdW heterostructures from this work and the literature.

Materials	Responsivity	Working wavelength	Bias condition	Reference
Si	0.75 A W^{-1}	200 – 560 nm	2 V	[1]
a-Si:H	0.15 A W^{-1}	260 nm	20 V	[2]
WS_2/Si	5.7 A W^{-1}	340 – 1100 nm	-5 V	[3]
MoS_2/GaAs	0.657 A W^{-1}	300 – 873 nm	-1 V	[4]
GaSe/WS_2	149 A W^{-1}	270 – 740 nm	2 V	[5]
GaSe/InSe	350 A W^{-1}	270 – 920 nm	2 V	[6]
GaSe/Ga_2O_3	51.9 A W^{-1}	< 280 nm	10 V	[7]
InSe/ReS_2	1921 A W^{-1}	365 – 965 nm	1 V	[8]
GaSe/In_2Se_3	145 A W^{-1}	325 – 1025 nm	3 V	This work

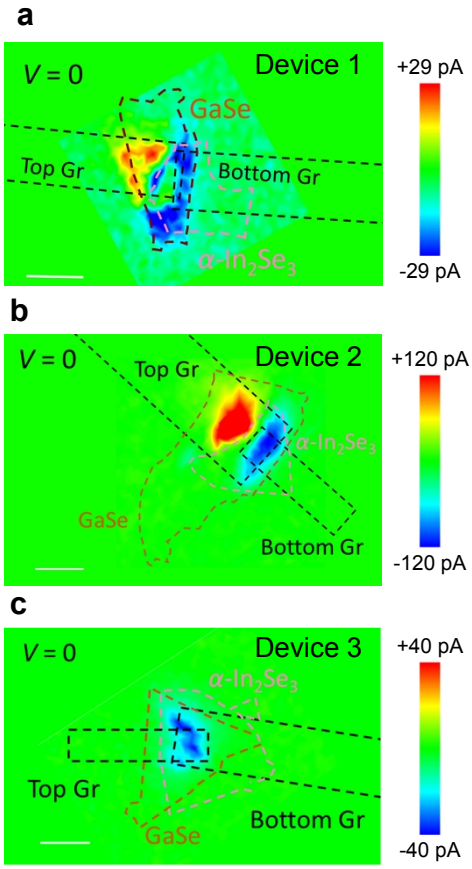

Supplementary Figure 5. Photocurrent maps of graphene-contacted *p*-GaSe/*n*-In_2Se_3 heterojunctions. (a-c) Room temperature (T = 300 K) photocurrent (ΔI) maps at V = 0 for three devices based on a graphene/*p*-GaSe/*n*-In_2Se_3/graphene heterojunction. The laser beam (λ = 405 nm) is focused by a microscope objective and the diameter of the spot size is around 1 μm. Scale bar: 10 μm.

Supplementary Note 1. Energy band diagrams of graphene-contacted *p*-GaSe/*n*-In_2Se_3 heterojunctions

To model the junction, we have assumed bulk crystals and treated the *pn*-junction and Schottky junctions in isolation. Parameters (carrier density and electron affinity) for pristine graphene are used for both Schottky contacts and any shift in the Fermi level of graphene due to charge transfer between the semiconductors and graphene is neglected.

Firstly, the energy step from (to) the valence (conduction) band in GaSe (In_2Se_3) to (from) the Fermi level is calculated using $V_p = k_B T ln\left(\frac{N_V}{p}\right) = 0.37$ eV ($V_n = k_B T ln\left(\frac{N_C}{n}\right) = 0.046$ eV), where N_V (N_C) is the density of states in the valence (conduction) band and is given by $N_V = 2\left(2\pi m^* k_B T / h^2\right)^{3/2}$ ($N_C = 2\left(2\pi m^* k_B T / h^2\right)^{3/2}$), where m^* is the effective mass of the majority carriers.

The Schottky barrier in GaSe is given by $\phi_{Bp} = E_{g,p} + \chi_p - \phi_m = 1.04$ eV, where the Fermi level in the graphene layers (as measured in graphene field effect transistors is 0.16 eV below the Dirac point, corresponding to a hole concentration of 1.17×10^{12} cm^{-2}) is treated as the work function of a metal, ϕ_m. The corresponding built-in potential is $V_{bi,p} = V_p - \phi_{Bp} = 0.67$ eV. The depletion region width in the GaSe is $x_p = \sqrt{\frac{2\epsilon_s(V_{bi,p} - V)}{qp}} = 8$ μm at zero bias, where ϵ_s is the dielectric permittivity of GaSe. A similar approach is used to calculate the corresponding parameters in In_2Se_3, giving $\phi_{Bn} = \phi_m - \chi_n = 1.06$ eV, $V_{bi,n} = \phi_{Bn} - V_n = 1.01$ eV and $x_n = \sqrt{\frac{2\epsilon_s(V_{bi,n} - V)}{qn}} = 54$ nm at zero bias.

The *pn*-junction has a built-in potential given by $V_{bi,pn} = E_{g,p} + \chi_p - \chi_n - V_n - V_p = 2.0 + 3.7 - 3.6 - 0.046 - 0.37 = 1.68$ eV.

The carrier concentration in In_2Se_3 is much higher than that in GaSe, so we treat the junction as one-sided and abrupt, with a depletion region entirely contained within the GaSe; $W = \sqrt{\frac{2\epsilon_s(V_{bi,pn} - V)}{qp}} = 10.7$ μm at $V = 0$.

Under an applied bias, it is assumed that the electric field is linear throughout the structure. The relative voltage drop across the junctions is therefore equivalent to their relative depletion widths in the case of a device with layer thicknesses equal to the combined depletion widths from each junction.

The resulting band diagrams for $V = 0$, $V = +1$ V and at the flat band condition for the *pn*-junction are in Supplementary Figure 6. The parameters used and calculated are shown in Supplementary Table 2.

The depletion widths in GaSe are much larger than in In_2Se_3 due to the much lower carrier concentration in GaSe. In forward bias, this results in a negligible change in the bending of the In_2Se_3 bands and in the right Schottky junction. In the GaSe, the forward bias reduces the height of the *pn*-junction barrier, reaching the flat band condition of $V_{bi,pn} = 1.68$ V at a total forward bias of $V \sim +3$ V. The reduction in barrier height is also accompanied by a decrease in the depletion width, reducing to zero at the flat band condition. The GaSe band bending near the GaSe/graphene interface increases under a forward bias.

Supplementary Table 2. Parameters of GaSe, In_2Se_3 and graphene used in the calculation of the energy band diagrams.

Properties	GaSe	In_2Se_3	Graphene	Reference
m^*	0.8 m_0	0.24 m_0	N/A	[9]
p (n)	1×10^{13} cm^{-3}	4.9×10^{17} cm^{-3}	1.17×10^{12} cm^{-2}	This work
χ	3.7 eV	3.6 eV	4.5 eV	[10-12]
E_g	2.0 eV	1.4 eV	N/A	This work
ε_s	6.18 ε_0	16.68 ε_0	N/A	[9]
Φ_B	1.04 eV	1.06 eV	N/A	This work
V_{bi}	0.67 eV	1.01 eV	N/A	This work
$W_{Schottky}(V = 0)$	8 μm	54 nm	N/A	This work
$W_{Schottky}(V = +1$ V)	8.67 μm	^	N/A	This work
$W_{Schottky}(V = +2.95$ V)	11.51 μm	^	N/A	This work

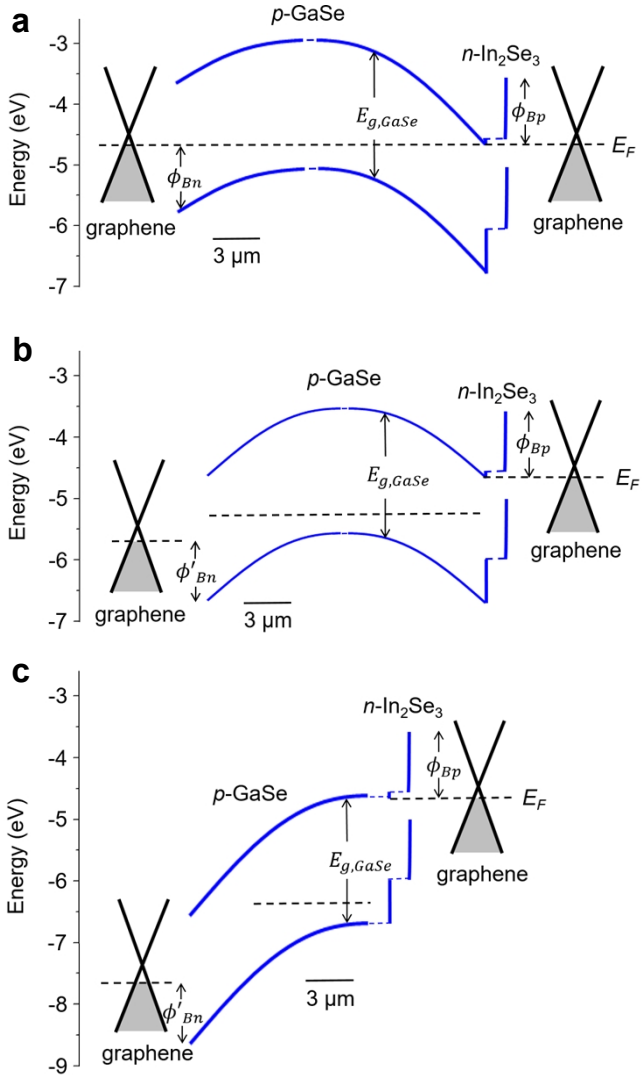

Supplementary Figure 6. Energy band diagrams. Energy band diagrams of graphene-contacted *p*-GaSe/*n*-In_2Se_3 heterojunctions at (a) $V = 0$, (b) $V = +1$ V and (c) $V = +2.95$ V. Blue dashed lines represent flat band regions of arbitrary length between the depletion regions.

Supplementary Note 2. Photoresponsivity under illumination with an unfocused and a focused laser beam

We estimated the responsivity of our devices under a focused laser at a fixed wavelength and different bias voltages. The responsivity values in the focused and unfocused mode versus the laser power density are plotted in Supplementary Figure 7. In the focused mode, the responsivity is calculated as the ratio between the current induced by light at one position (area $A = \pi d^2/4 \sim 1.5$ μm^2, diameter $d = 1.22\lambda/\mathrm{NA} = 1.4$ μm, where NA = 0.35 is the numerical aperture and $\lambda = 405$ nm) and the incident power. Since the photocurrent is non-uniform, we illustrate the responsivity data as a vertical line, spanning the lowest and highest responsivity values at different positions. The line is centred around the average responsivity. To estimate R at each position, we subtracted from the measured current the dark current over the same area of the laser spot. The data show that the responsivity in the focused laser mode is in line with data for the unfocused mode: the value of R tends to decrease with increasing power density. This non-linear response is similar to that reported for many photodetectors in the literature [13-16]. An increasing power density tends to increase the carrier recombination rate due to an increase density of photogenerated carriers.

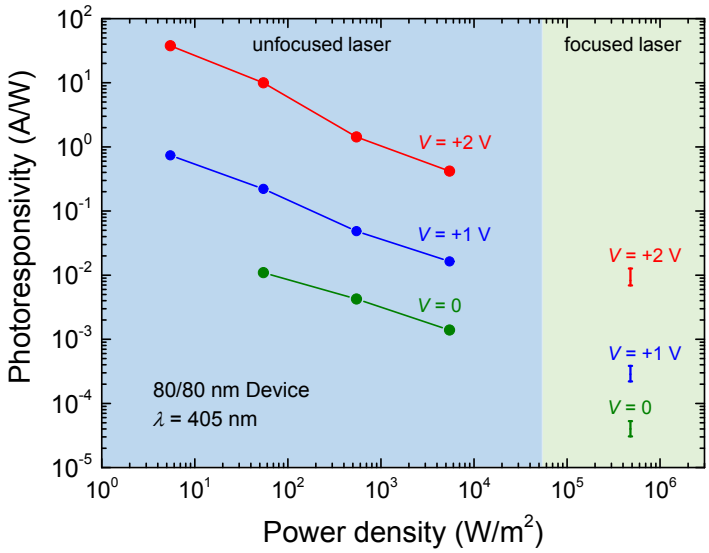

Supplementary Figure 7. Photoresponse under unfocused/focused laser beam. Photoresponsivity versus laser power density for different applied voltages V under an unfocused (dots) and a focused (vertical lines) laser beam for a graphene contacted p-GaSe/n-In_2Se_3 junction (80/80 nm).

Supplementary Note 3. Laser annealing of GaSe flakes

A focused laser beam with a diameter of ~ 1 μm, power $P > 0.5$ mW and $\lambda = 532$ nm was used to anneal a GaSe flake for a time interval in the range $\Delta t = 10$ s to 60 s. After each annealing, the sample was allowed to cool down for approximately 20 s before conducting PL and Raman measurements. All measurements were taken on the same point of the flake at $T = 300$ K. Supplementary Figure 8 shows the PL (a) and Raman (b) spectra of a GaSe flake before and after laser annealing at $T = 300$ K. The time for each curve shows the total annealing time at the given laser power. Following a prolonged laser annealing, the band edge PL emission weakens and is replaced by a broad PL emission peaked at ~ 1.7 eV. The strengthening of the Raman line at 255 cm^{-1} following the annealing is attributed to the local photo-oxidation of the flake due to the formation of amorphous selenium (α-Se) [17].

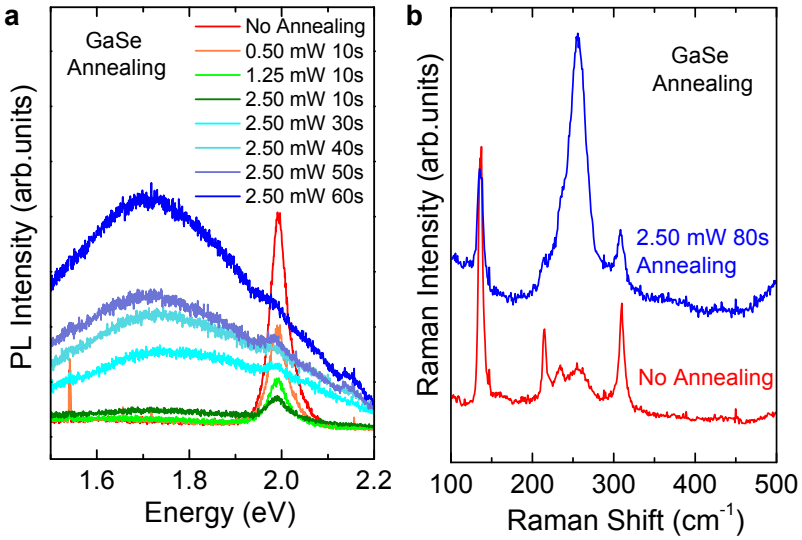

Supplementary Figure 8. PL and Raman spectra of a GaSe flake. (a) PL spectra of a GaSe flake before and after laser annealing in air with different powers/annealing times ($T = 300$ K, $\lambda = 532$ nm). (b) Raman spectra of a GaSe flake before and after annealing ($T = 300$ K, $\lambda = 532$ nm). The enhancement of the peak at 255 cm^{-1} is attributed to the photo-oxidation of GaSe [17].

Supplementary Note 4. Stability tests

Since GaSe can oxidize in air, leading to morphological and chemical changes of its surface, our device studies were conducted in vacuum and at laser powers that avoid light-induced changes of GaSe. Examples of the stability tests for our devices under these conditions are in Supplementary Figure 9. The measured current remains stable over time, switching between high to low (dark current) values in response to the impinging laser power.

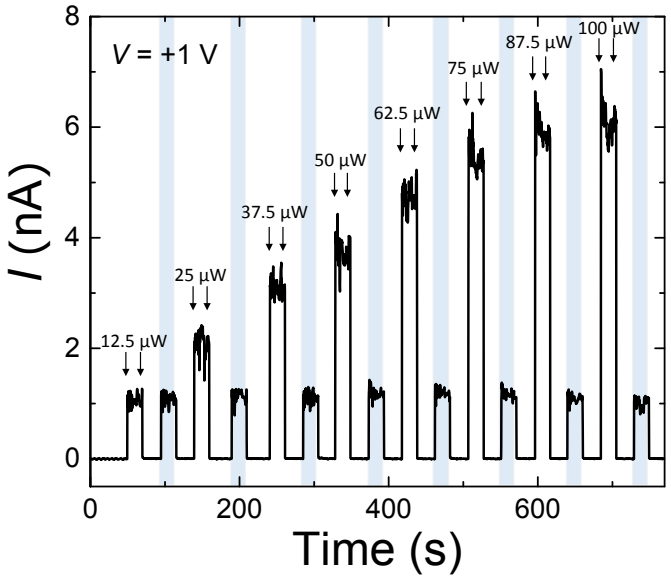

Supplementary Figure 9. Stability tests. Temporal dependence of the current for a graphene contacted *p*-GaSe/*n*-In_2Se_3 junction (80/80 nm) in the dark, laser power $P = 12.5$ μW (blue) and exposure to laser with increasing powers (from 12.5 μW to 100 μW, as indicated by arrows) ($T = 300$ K, $\lambda = 405$ nm, $V = +1$ V).

Supplementary References

1 Nayfeh, O. M., Rao, S., Smith, A., Therrien, J. & Nayfeh, M. H. Thin Film Silicon Nanoparticle UV Photodetector. *IEEE Photon. Technol. Lett.* **16**, 1927-1929 (2004).

2 Khodami, I., Taghibakhsh, F. & Karim, K. S. UV-Enhanced a-Si:H Metal–Semiconductor–Metal Photodetector. *IEEE Electron Device Lett.* **29**, 1007-1010 (2008).

3 Lan, C. *et al.* Zener Tunneling and Photoresponse of a WS_2/Si van der Waals Heterojunction. *ACS Appl. Mater. Interfaces* **8**, 18375-18382 (2016).

4 Xu, Z. *et al.* Monolayer MoS_2/GaAs heterostructure self-driven photodetector with extremely high detectivity. *Nano Energy* **23**, 89-96 (2016).

5 Lv, Q., Yan, F., Wei, X. & Wang, K. High-Performance, Self-Driven Photodetector Based on Graphene Sandwiched GaSe/WS_2 Heterojunction. *Adv. Opt. Mater.* **6**, 1700490 (2018).

6 Yan, F. *et al.* Fast, multicolor photodetection with graphene-contacted *p*-GaSe/*n*-InSe van der Waals heterostructures. *Nanotechnology* **28**, 27LT01 (2017).

7 Wang, Y. *et al.* *p*-GaSe/*n*-Ga_2O_3 van der Waals Heterostructure Photodetector at Solar-Blind Wavelengths with Ultrahigh Responsivity and Detectivity. *ACS Photonics* **8**, 2256-2264 (2021).

8 Ma, H. *et al.* Ultrasensitive and Broad-Spectrum Photodetectors Based on InSe/ReS_2 Heterostructure. *Adv. Opt. Mater.* **10**, 2101772 (2022).

9 Madelung, O. *Semiconductors: data handbook*. (Springer Science & Business Media, 2004).

10 Drapak, S., Kovalyuk, Z., Netyaga, V. & Orletskii, V. On the mechanisms of current transfer in *n*-In_2Se_3-*p*-GaSe heterostructures. *Tech. Phys. Lett* **28**, 707-710 (2002).

11 Jaegermann, W., Klein, A. & Pettenkofer, C. in *Electron Spectroscopies Applied to Low-Dimensional Materials* 317-402 (Springer, 2002).

12 Mudd, G. W. *et al.* High broad-band photoresponsivity of mechanically formed InSe–graphene van der Waals heterostructures. *Adv. Mater.* **27**, 3760-3766 (2015).

13 Xie, S. *et al.* Ferroelectric semiconductor junctions based on graphene/In_2Se_3/graphene van der Waals heterostructures. *2D Mater.* **8**, 045020 (2021).

14 Island, J. O., Blanter, S. I., Buscema, M., van der Zant, H. S. & Castellanos-Gomez, A. Gate controlled photocurrent generation mechanisms in high-gain In_2Se_3 phototransistors. *Nano Lett.* **15**, 7853-7858 (2015).

15 Cao, Y. *et al.* Strong enhancement of photoresponsivity with shrinking the electrodes spacing in few layer GaSe photodetectors. *Sci. Rep.* **5**, 8130 (2015).

16 Sorifi, S., Moun, M., Kaushik, S. & Singh, R. High-Temperature Performance of a GaSe Nanosheet-Based Broadband Photodetector. *ACS Appl. Electron. Mater.* **2**, 670-676 (2020).

17 Rahaman, M., Rodriguez, R. D., Monecke, M., Lopez-Rivera, S. A. & Zahn, D. R. T. GaSe oxidation in air: from bulk to monolayers. *Semicond. Sci. Technol.* **32**, 105004 (2017).